Phase-field Model for Interstitia Loop Growth Kinetics and Thermodynamic and Kineti Models of Irradiated Fe-Cr Allo

Fuel Cycle Research & Development

Prepared for

U.S. Department of Energy

Fuel Cycle R&D Program

Yulan Li, Shenyang Hu, Xin Sun and Moe Khaleel

Pacific Northwest National Laboratory, Richland, WA 99352

May 2011

FCRD- NEAMS-2011-000125

PNNL-20467

Reviewed by:

Acting Director, Fuel Cycle Research and Development

Robert Price Date

Concurred by:

Director, Advanced Fuel Cycle Initiative Technical Integration Office

Phillip Finck Date

Approved by:

Deputy Assistant Secretary, Fuel Cycle Management

(AFCI Program Manager) Paul Lisowski Date

SUMMARY

Microstructure evolution kinetics in irradiated materials has strong spatial correlation. For example, voids and second phases prefer to nucleate and grow at pre-existing defects such as dislocations, grain boundaries, and cracks. Inhomogeneous microstructure evolution results in inhomogeneity of microstructure and thermomechanical properties. Therefore, the simulation capability to predict three-dimensional (3-D) microstructure evolution kinetics and its subsequent impact on material properties and performance is crucial for scientific design of advanced nuclear materials and optimal operation conditions and for reducing uncertainty in operational and safety margins.

Recently, mesoscale phase-field (PF) models have been developed to predict gas bubble evolution, void swelling, void-lattice formation and void migration in irradiated materials. Although most phase-field simulations are qualitative today due to the lack of accurate thermodynamic and kinetic properties of defects, and the scalability limitations of current research codes on high performance computers for large time and length scale simulations, PF method has demonstrated itself as one of the promising simulation tools for predicting 3-D heterogeneous microstructure and property evolution, and for providing microstructure evolution kinetics for higher-scale simulations of microstructure and property evolution.

This report consists of two parts. In Part I, we present a new phase-field model for predicting interstitial loop growth kinetics in irradiated materials. The model takes into account the effects of defect (vacancy/interstitial) generation, diffusion and recombination, sink strength, long-range elastic interaction, and inhomogeneous and anisotropic mobility on microstructure evolution kinetics. The model is used to study the influence of elastic interaction on interstitial loop growth kinetics, the interstitial flux, and the sink strength of interstitial loops for interstitials. In Part II, we present a generic phase-field model and discuss the thermodynamic and kinetic properties in phase-field models including the reaction kinetics of radiation defects and local free energy of irradiated materials. In particular, a two-sublattice thermodynamic model is suggested to describe the local free energy of alloys with irradiated defects. An Fe-Cr alloy is taken as an example to explain the required thermodynamic and kinetic properties for quantitative phase-field modeling. Finally the great challenges in phase-field modeling will be discussed.

CONTENTS

FIGURES

TABLES

ACRONYMS

1-D	one-dimensional
3-D	three-dimensional
bcc	body-centered cubic
CALPHAD	CALculation of PHAse Diagrams
MD	Molecular Dynamics
PF	Phase-Field
PNNL	Pacific Northwest National Laboratory
RT	rate theory
SIA	self-interstitial atom

FUEL CYCLE R&D PROGRAM
Phase-field Model for Interstitial Loop Growth Kinetics and Thermodynamic and Kinetic Models of Irradiated Fe-Cr Alloys

1. INTRODUCTION

Complex microstructure evolutions occur in nuclear fuels and/or structural components in operating nuclear reactors due to fission products and radiation damage. These microstructure evolutions include the formation of voids or gas bubbles, recrystallization, precipitation, solute segregation, oxidation and corrosion, etc, and they affect the materials' thermo-mechanical properties and result in structural instability including volume swelling and cracking. Extensive experiments demonstrated that the microstructure evolution kinetics in irradiated materials has strongly spatial correlation.[1-3] For example, radiation-induced segregation near grain boundaries, enhanced swelling, void supper-lattices, and heterogeneous nucleation and growth of second phases at pre-existing defects (such as dislocations, grain boundaries, and cracks) are observed in the materials under neutron or heavy-ion irradiation. The heterogeneous microstructures eventually determine the material performance. Therefore, predicting microstructure evolution kinetics and its subsequent impact on material properties and performance is crucial for scientific design of advanced nuclear materials and optimal operating conditions and for reducing uncertainty in operational and safety margins.

Microstructure evolution in irradiated materials is a very complicated process that involves defect generation, migration and reaction, nucleation of new defects/phases such as dislocations, voids, gas bubbles, and precipitates, defect/phase growth and coarsening. The evolution process spans large time and length scales. Extensive effort has been made in modeling microstructure evolution in irradiated materials over the past 40 years. On the atomistic scale, the molecular dynamic (MD) method has been successfully used to study defect generation during cascades, defect migration, and the interaction between structural defects and irradiation defects.[4-7] The kinetic Monte Carlo method[8-10] and object kMC method[11] have been proposed to investigate defect migration and microstructure evolution. Atomistic simulations revealed the thermodynamic and kinetic properties of point defects in various crystals under irradiation. On the macro-scale, based on a mean-field approximation of reaction kinetics with the generation of defects, rate theory (RT) models [12, 13] have been developed to a great extent in an attempt to explain the variety of phenomena observed: radiation-induced hardening, creep, swelling, segregation and second-phase precipitation. However, the models did not take into account the spatial arrangement of irradiation defects and microstructure as well as the inhomogeneity and anisotropy of defect mobility. The Production Bias Model (PBM)[14-20] is a generalization of rate theory that accounts for more features of irradiation defects such as the production of point defect clusters, the one-dimensional (1-D) diffusion of self-interstitial atom (SIA) clusters, the reaction rate between 1-D migrating clusters and immobile sinks, and the recoil energy dependence of defect profiles. Although the mean-field models can deal with the microstructure evolution with a time scale spanning from atomic events such as small defect nucleation to macro-scale process including void swelling and creep, their predictive capability relies on the fundamental understanding and accurate reaction kinetics of defects. The reaction kinetics such as the generation rate of defect and defect clusters, nucleation rates of second phases, and defect mobility has

strong spatial correlation. Mesoscale simulation methods such as OkMC[11], Potts model[21], and phase-field (PF) model[22], which take into account 3-D inhomogeneous microstructure and 3-D reaction kinetics, can provide the microstructure evolution kinetics for the mean field models.

The PF method based on the fundamental thermodynamic and kinetic information has been emerging as a powerful computational approach at the meso scale for predicting phase stability and microstructural evolution kinetics during many materials processes such as solidification, precipitation in alloys, ferroelectric domain evolution in ferroelectric materials, martensitic transformation, dislocation dynamics, and electrochemical process[23-27]. This method describes a microstructure using a set of conserved and nonconserved variables that are continuous across the interfacial regions. The temporal and spatial evolution of the variables, i.e., the microstructural evolution, is governed by the Cahn-Hilliard nonlinear diffusion equation and the Alan Cahn relaxation equation. It uses input of thermodynamic and kinetic data from atomistic simulations, thermodynamic calculations and experiments, and outputs kinetic information of microstructure evolution.

Very recently the application of phase-field modeling has been extended into irradiated materials. Reaction kinetics of radiation kinetics, heterogeneous and homogeneous nucleation, 1-D migration of SIAs, inhomogeneous mobility, the Sorét effect, anisotropic interfacial energy, and long-range elastic interaction have been integrated into phase-field models for investigating the microstructure evolution in nuclear fuels and cladding materials.[28-33] A general phase-field model was proposed to simulate gas bubble evolution in a polycrystalline material with defects.[28, 29] The model considered two phases coexisting, i.e., a matrix phase with the generation of fission gas atoms, and a fission gas phase. Elastic interactions among defects such as dislocations, grain boundaries, small vacancy clusters, and fission gas atoms were taken into account in addition of the equation of state of the gas phase. It enables one to investigate the heterogeneous nucleation of gas bubbles on dislocations, grain boundaries, and small vacancy clusters and to study the effect of radiation conditions, dislocation distributions, and grain sizes on gas bubble microstructure and evolution kinetics. The evolving gas bubble microstructure from the simulations can be used to evaluate the effect of microstructure on thermal conductivity. In irradiated materials the two features play an important role in the microstructure evolution. One feature is that self-interstitials migrate along close packing directions of crystals. The other one is that the mobility of interstitials is much larger than that of vacancies. A phase-field model integrating 3-D vacancy diffusion and 1-D migration of SIAs was proposed to account for these two important features.[30] The critical conditions for the formation of void lattices and the effect of radiation rates on void lattice morphology were examined with the developed model for a given crystal. Temperature gradient in nuclear components in operating nuclear reactors causes defect migration, i.e., the so-called Sorét effect. The inhomogeneous mobility of vacancies in bulk and surfaces was considered in a phase-field model by Hu and Henager[31] and Li et al.[32] The model can be used to study the migration mobility of a single void and the effect of temperature gradient and reaction kinetics of radiation defects. Void swelling kinetics was studied by the phase-field method as well by accounting for the competition between void nucleation and vacancy diffusion.[33] A bell-shaped temperature dependence of void swelling was predicted with the model, which is in agreement with the experimental observation. Although most results of the phase-field simulations are qualitative due to the lack of accurate thermodynamic and kinetic properties of defects, possible missing of important kinetic properties and processes, and the limitations of current codes and computers for large time- and length-scale modeling, the simulations have demonstrated that the PF method is a promising simulation tool for predicting the 3-D heterogeneous microstructure and property

evolution, and able to provide the microstructure evolution kinetics for higher level simulations in large time and length scales about microstructure and property evolution such as mean field methods.

This report includes two parts. In Part I, we present a new phase-field model for predicting interstitial loop growth kinetics in irradiated materials. The effects of defect (vacancy/interstitial) generation, diffusion and recombination, sink strength, long-range elastic interaction, and inhomogeneous and anisotropic mobility on microstructure evolution kinetics are taken into account in the model. The model is used to study the effect of elastic interaction on interstitial loop growth kinetics, the interstitial flux, and the sink strength of interstitial loops for interstitials. In Part II, we present a generic phase-field model of multi-phase evolution in Fe-Cr alloys and discuss the thermodynamic and kinetic properties in a phase-field model including the reaction kinetics of radiation defects and local free energy of irradiated materials. In particular, a two-sublattice thermodynamic model is suggested to describe the local free energy of alloys with irradiated defects. Finally, the great challenges ahead in phase-field modeling will be discussed.

2. PART I: PHASE-FIELD MODEL FOR INTERSTITIAL LOOP EVOLUTION KINETICS IN BCC IRON

Interstitial loops are one of the important sinks for SIAs. Experimental observations[34-37] and atomistic simulation studies[38, 39] demonstrated that two kinds of interstitial loops with Burgers vector $\mathbf{b} = a < 100 >$ on $\{100\}$ planes and Burgers vector $\mathbf{b} = a/2 < 111 >$ on $\{110\}$ planes, (where a is the lattice constant), exist in ferritic steels. Experiments and molecular dynamic (MD) simulations have also shown that interstitial loops with $\mathbf{b} = a < 100 >$ have a strong bias for SIAs as well as solutes.[40-42] Formation mechanisms of interstitial loops with $\mathbf{b} = a < 100 >$ have been studied using MD and experiments.[42, 43] In this work, we developed a phase-field model to study the stability and growth kinetics of an interstitial loop with $\mathbf{b} = a < 100 >$ in an irradiated body-centered cubic (bcc) metal. The details of the model and simulation results are shown in the following sections.

2.1 Description of phase-field model

Here we consider the interstitial loops with Burgers vectors $\mathbf{b} = a < 100 >$ on $\{100\}$ planes and study their evolution in irradiated bcc materials. We view all mobile vacancies and small vacancy clusters as single vacancies with effective concentration and mobility. Mobile interstitials and small interstitial clusters are construed as single interstitials with their effective concentrations and mobilities. The interstitial loops are assumed to be immobile. Therefore, five phase-field variables are used to describe the microstructural features: $c_I(\mathbf{r},t)$ and $c_V(\mathbf{r},t)$ for SIA and vacancy concentrations, respectively, and three order parameters $\eta_m(\mathbf{r},t)$, $m = 1,2,3$, for three different orientations of the interstitial loops with Burgers vectors $\mathbf{b} = a < 100 >$, where $\mathbf{r}$=(r_1, r_2, r_3) is the spatial coordinate and t is time. The interstitial loops are viewed as disc-shaped precipitates that consist of 100% SIAs. A perfect interstitial loop in bcc metals consists of two SIA layers as depicted by Wirth[44], and has its equilibrium SIA concentration of $c_I^{eq}(T) = 1$ and equilibrium vacancy concentration of $c_V^{eq}(T) = 0$. The order parameter $\eta_m(\mathbf{r},t)$ is equal to 1 inside the interstitial loop and 0 outside, and it changes smoothly from 0 to 1 across the interface between the interstitial loop and matrix. The solubilities of vacancies and SIAs in the matrix depend on

temperature *T*, and are denoted as $c_I^{eq0}(T)$ and $c_V^{eq0}(T)$, respectively. The free energy of the system, including the chemical free energy $f(c_I, c_V, \eta_m, T)$, interfacial energy E^{inter} and elastic energy E^{elast}, can be written as

$$F = \iiint_V \left[f(c_I, c_V, \eta_m, T) + E^{inter} + E^{elast} \right] dV . \quad (1)$$

The diffusion of vacancies and interstitials are described by the Cahn-Hilliard equations:[45]

$$\frac{\partial c_V}{\partial t} = \nabla \cdot \left[M_V \nabla \frac{\delta F}{\delta c_V} \right] + \dot{g}_V(\mathbf{r}, t) + \dot{R}_{IV}(\mathbf{r}, t) + \dot{s}_V(\mathbf{r}, t) , \quad (2)$$

$$\frac{\partial c_I}{\partial t} = \nabla \cdot \left[M_I \nabla \frac{\delta F}{\delta c_I} \right] + \dot{g}_I(\mathbf{r}, t) + \dot{R}_{IV}(\mathbf{r}, t) + \dot{s}_I(\mathbf{r}, t) , \quad (3)$$

where M_V and M_I are the mobilities of vacancies and interstitials, respectively. The variables $\dot{g}_{I,V}$, $\dot{R}_{IV}$, and $\dot{s}_{I,V}$ are the generation rate, recombination rate, and sink strength of vacancies and interstitials, respectively. The generation rate[46] can be calculated by $\dot{g}_I = \dot{g}_V \approx d(dpa)/dt$, where *dpa* denotes the displacements per atom. The recombination rate[47] is generally given by $\dot{R}_{IV} = -6Z_{IV}(D_I + D_V)c_I c_V / \lambda^2$, where D_I and D_V are the diffusivities of the interstitials and vacancies, respectively, and Z_{IV} (the recombination cross section) is a constant in the range 3.3~7.2. λ is the jump distance. The sink strengths are calculated by $\dot{s}_I = -k_I D_I (c_I - c_I^{eq0})$ and $\dot{s}_V = -k_V D_V (c_V - c_V^{eq0})$ where the coefficients k_I and k_V depend on the type and density of sinks[48, 49].

The evolution rate of the order parameters is assumed to be a linear function of the thermodynamic driving forces. The simplest form of the kinetic equation is the time-dependent Ginzburg-Landau equation:[50]

$$\frac{\partial \eta_m}{\partial t} = -L \frac{\delta F}{\delta \eta_m}, \qquad (m = 1, 2, 3) , \quad (4)$$

where L is the kinetic coefficient characterizing the interface mobility of the interstitial loops. In Eqs. (2-4), *F* is the total energy given in Eq. (1). $\delta F / \delta X$, $(X = c_I, c_V, \eta_m)$, is the variational derivative of *F* with respect to variable *X*, *i.e.*, the thermodynamic driving force.

The Kim's model[26] is employed to construct the system chemical free energy. One advantage of the Kim's model is that a larger grid size can be used in simulations for given interfacial energy and interface mobility. In consequence, larger time and length scales can be reached in the simulations. Following the Kim's model, the chemical free energy as a function of the concentrations and order parameters is described as

$$f(c_I, c_V, \eta_m, T) = h(\eta_1, \eta_2, \eta_3) f_M(c_I, c_V, T) + [1 - h(\eta_1, \eta_2, \eta_3)] f_L(c_I, c_V, T) + w g(\eta_1, \eta_2, \eta_3) , \quad (5)$$

where $f_M(c_I, c_V, T)$ and $f_L(c_I, c_V, T)$ are the free energies of the matrix phase and the interstitial loop phase, respectively. $h(\eta_1, \eta_2, \eta_3) = \sum_m 3\eta_m^2 - 2\eta_m^3$ is a shape function that represents the volume fraction of the matrix and interstitial loop phases at a spatial point **r**. $g(\eta_1, \eta_2, \eta_3) = \sum_m \eta_m^2(1-\eta_m^2)$ is a double well potential, and w is the height of the double well. Taking the unirradiated material as the reference state, the free energy of the matrix phase $f_M(c_I, c_V, T)$ with vacancies and SIAs can be described by

$$f_M(c_I, c_V, T) = f_M^0(T) + H(c_I, c_V) - TS(c_I, c_V), \tag{6}$$

where $f_M^0(T)$ is the free energy of the reference state. It can be obtained from phase diagram calculations such as CALPHAD. $H(c_I, c_V)$ and $S(c_I, c_V)$ are the enthalpy and entropy changes due to the introduction of defects at temperature *T*. Generally, the enthalpy change can be expressed by a polynomial in terms of vacancy and interstitial concentrations while the entropy change can be described as $S(c_I, c_V) = k_B \ln W$. k_B is the Boltzmann constant and W is the thermodynamic probability as a possible combination of the numbers of vacancies, interstitials and lattice atoms of the system. In the dilute solution limit, $f_M(c_I, c_V, T)$ can be written as

$$\begin{aligned} f_M(c_I, c_V, T) = {} & f_M^0(T) + \\ & + \frac{N}{\Omega}\left\{E_V^f c_V + E_I^f c_I - k_B T[c_I \ln c_I + (1-c_I)\ln(1-c_I) + c_V \ln c_V + (1-c_V)\ln(1-c_V)]\right\}, \end{aligned} \tag{7}$$

where E_V^f and E_I^f are the vacancy and interstitial formation energies, respectively. N is the Avogadro constant, and Ω is the molar volume. The Kim's model assumes that at each point **r** the matrix and interstitial loop phases have the same chemical potentials but different concentrations, i.e., (c_I^M, c_V^M) for the matrix and (c_I^L, c_V^L) for the interstitial loop phase, respectively. This implies that the conditions:

$$\partial f_M(c_I^M, c_V^M, T)/\partial c_I = \partial f_L(c_I^L, c_V^L, T)/\partial c_I,\ \partial f_M(c_I^M, c_V^M, T)/\partial c_V = \partial f_L(c_I^L, c_V^L, T)/\partial c_V, \tag{8a}$$

$$h(\eta_1, \eta_2, \eta_3)c_I^M + [1 - h(\eta_1, \eta_2, \eta_3)]c_I^L = c_I,\ \ h(\eta_1, \eta_2, \eta_3)c_V^M + [1 - h(\eta_1, \eta_2, \eta_3)]c_V^L = c_V, \tag{8b}$$

should be satisfied during microstructure evolution. The free energy of the interstitial loops $f_L(c_I, c_V, T)$ is assumed as,

$$f_L(c_I, c_V, T) = f_L^0(T) + A_L[(c_I - c_I^{eq}(T))^2 + (c_V - c_V^{eq}(T))^2]. \tag{9}$$

The coefficient A_L and f_L^0 can be determined by the equilibrium thermodynamic properties that the free energies $f_M(c_I, c_V, T)$ and $f_L(c_I, c_V, T)$ have a common tangent at their equilibrium concentrations.

For alloys, $f_M^0(T)$ should depend on alloy concentrations. Since the radiation defects (vacancies and interstitials) occupy the host and interstitial lattices, a general two-sublattice thermodynamic model with multi-components can be used to describe the enthalpy and entropy changes for the alloy system.[51, 52]

The second term on the right side of Eq. (1) is the gradient energy associated with the interfacial energy of the interstitial loops. The interfacial energy of the broad in-plane interfaces of the loop depends on whether the loop is a perfect loop or a faulted loop; however, it should be much smaller than that along the rim of the loop. In order to describe the strong anisotropy of the interfacial energy, we separate the interfacial energy into two parts as

$$E^{inter} = \sum_m \frac{\kappa}{2}\left|\nabla \eta_m\right|^2 + \sum_m \frac{\kappa_1}{2}\left|\mathbf{n}_m \times \nabla \eta_m\right|^2 \quad . \tag{10}$$

The first term on the right side of Eq. (10) describes the isotropic interfacial energy. The coefficient κ together with the double-well height w of Eq. (5) can be determined by the interfacial energy and interface thickness of the broad interface of the loop. Since we consider a perfect interstitial loop, the interfacial energy of the broad interface of the loop is zero. Therefore, $\kappa = 0$ is used in the simulations and w is chosen to ensure the free energy presenting two phases coexisting. The second term describes the interfacial energy along the rim of the loop with $\mathbf{n}_m$ being its unit normal vector. This term is zero on the planar interface because $\mathbf{n}_m$ and $\nabla \eta_m$ are parallel vectors. The coefficient κ_1 is associated with the interstitial loop core energy γ_{dis} by $\kappa_1 \approx \gamma_{dis} r_0 / d_0$, where r_0 is the dislocation core radius, and d_0 is the interplanar distance of the dislocation slip plane. γ_{dis} can be calculated from atomistic simulations.[53-55]

The last term in Eq. (1) is the elastic energy. If the variation of the stress-free lattice parameter, a, with given defect (vacancy and interstitial) concentrations is assumed to obey Vegard's law, the local stress-free strain caused by the defect inhomogeneity is given by

$$\varepsilon_{ij}^{VI*} = \varepsilon^{V0}\left(c_V - c_V^{eq0}\right)\delta_{ij} + \varepsilon^{I0}\left(c_I - c_I^{eq0}\right)\delta_{ij}, \tag{11}$$

where $\varepsilon^{V0} = (1/a)da/dc_V$ and $\varepsilon^{I0} = (1/a)da/dc_I$ are the expansion coefficients of the lattice parameter due to the introduction of vacancies and interstitials, respectively, and δ_{ij} is the Kronecker-delta function. However, since the interstitial concentration is equal to 1 inside an interstitial loop, Vegard's law may no longer be applicable. Thus, an additional term is used for correction

$$\varepsilon_{ij}^{*L}(\mathbf{r}) = \frac{\varepsilon^{L0}}{2}\sum_m \left\{n_m(i)n_m(j) + n_m(j)n_m(i)\right\}\eta_m(\mathbf{r}), \tag{12}$$

where ε^{L0} describes the change of the interplanar distance due to the interstitial loop and $n_m(i)$, (i=1, 2, 3) is the component of the unit vector $\mathbf{n}_m$. Therefore, the total stress-free strain tensor is

$$\varepsilon_{ij}^{*} = \varepsilon_{ij}^{VI*} + \varepsilon_{ij}^{*L} = \varepsilon^{V0}\left(c_V - c_V^{eq0}\right)\delta_{ij} + \varepsilon^{I0}\left(c_I - c_I^{eq0}\right)\delta_{ij} + \sum_m [\frac{\varepsilon^{L0}}{2}\{n_m(i)n_m(j) + n_m(j)n_m(i)\} - \varepsilon^{I0}\left(c_I - c_I^{eq0}\right)\delta_{ij}]\eta_m . \quad (13)$$

The elastic energy density E^{elast} can be calculated by:[56]

$$E^{elast} = \frac{1}{2}\lambda_{ijkl}\varepsilon_{ij}^{el}\varepsilon_{kl}^{el} , \quad (14)$$

where the summation convention over i, j, k, l (i, j, k, l=1, 2, 3) is used. λ_{ijkl} is the elastic constant tensor and ε_{ij}^{el} is the elastic strain given by

$$\varepsilon_{ij}^{el} = \bar{\varepsilon}_{ij} + \delta\varepsilon_{ij}(\mathbf{r}) - \varepsilon_{ij}^{*}(\mathbf{r}) , \quad (15)$$

where $\bar{\varepsilon}_{ij}$ is the homogeneous macroscopic strain characterizing the macroscopic shape and volume change and $\delta\varepsilon_{ij}(\mathbf{r})$ is the heterogeneous strain which satisfies $\int_V \delta\varepsilon_{ij}(\mathbf{r})dV = 0$. The elastic strain ε_{ij}^{el} can be obtained by solving the mechanical equations of $\sigma_{ij,j} = 0$ with σ_{ij} being the stress component and $\sigma_{ij} = \lambda_{ijkl}\varepsilon_{kl}^{el}$. For elastic inhomogeneous solids, such as polycrystalline materials, the elastic solution can be obtained using an iteration method.[57]

We use the following normalizations for our numerical calculations: $t^{*} = (C_{44}M_{I0}/l_0^2)t = t/t_0$, $t_0 = l_0^2/(C_{44}M_{I0})$, $M_{I0} = D_{I0}\Omega/(T\Re)$, $r_i^{*} = r_i/l_0$ $M_V^{*} = M_V/M_{I0}$, $M_I^{*} = M_I/M_{I0}$, $L^{*} = Ll_0^2/M_{I0}$, $f^{*} = f/C_{44}$, $w^{*} = w/C_{44}$, $A_L^{*} = A_L/C_{44}$, $\kappa^{*} = \kappa/(l_0^2C_{44})$, $\kappa_1^{*} = \kappa_1/(l_0^2C_{44})$, $\sigma_{ij}^{*} = \sigma_{ij}/C_{44}$, $\dot{g}_{I,V}^{*} = \dot{g}_{I,V}t_0$, $\gamma^{*} = -6Z_{IV}D_It_0/\lambda^2$, $k_I^{*} = k_ID_It_0$, and $k_V^{*} = k_VD_Vt_0$ with l_0 being a characteristic length and D_{I0} being the interstitial diffusivity at a given temperature T_0. $\Re$ is the ideal gas constant and C_{44} is the shear modulus of the considered material. With $\nabla = (\partial/\partial r_1, \partial/\partial r_2, \partial/\partial r_3)$ $= (\partial/\partial r_1^{*}, \partial/\partial r_2^{*}, \partial/\partial r_3^{*})/l_0 = \nabla^{*}/l_0$, we obtain the following dimensionless equations:

$$\frac{\partial c_V}{\partial t^{*}} = M_V^{*}\nabla^{*2}\left(\frac{\partial f^{*}}{\partial c_V} - \sigma_{ij}^{*}\frac{\partial \varepsilon_{ij}^{*}}{\partial c_V}\right) + \dot{g}_V^{*} + \gamma^{*}(1 + D_V/D_I)c_Ic_V + k_V^{*}(c_V - c_V^{eq0}) , \quad (16)$$

$$\frac{\partial c_I}{\partial t^{*}} = M_I^{*}\nabla^{*2}\left(\frac{\partial f^{*}}{\partial c_I} - \sigma_{ij}^{*}\frac{\partial \varepsilon_{ij}^{*}}{\partial c_I}\right) + \dot{g}_I^{*} + \gamma^{*}(1 + D_V/D_I)c_Ic_V + k_I^{*}(c_I - c_I^{eq0}) , \quad (17)$$

$$\frac{\partial \eta_m}{\partial t^*} = -L^*\left(\frac{\partial f^*}{\partial \eta_m} - \kappa^*\nabla^{*2}\eta_m + \sigma_{ij}^*\frac{\partial \varepsilon_{ij}^*}{\partial \eta_m}\right)$$
$$+ L^*\kappa_1^*\left\{(n_m(1))^2\left(\frac{\partial^2\eta_m}{\partial r_2^{*2}} + \frac{\partial^2\eta_m}{\partial r_3^{*2}}\right) + (n_m(2))^2\left(\frac{\partial^2\eta_m}{\partial r_1^{*2}} + \frac{\partial^2\eta_m}{\partial r_3^{*2}}\right) + (n_m(3))^2\left(\frac{\partial^2\eta_m}{\partial r_2^{*2}} + \frac{\partial^2\eta_m}{\partial r_1^{*2}}\right)\right\} \quad (18)$$
$$- 2L^*\kappa_1^*\left\{n_m(1)n_m(2)\frac{\partial^2\eta_m}{\partial r_1^*\partial r_2^*} + n_m(2)n_m(3)\frac{\partial^2\eta_m}{\partial r_2^*\partial r_3^*} + n_m(3)n_m(1)\frac{\partial^2\eta_m}{\partial r_3^*\partial r_1^*}\right\}, \quad m = 1,2,3.$$

By solving Eqs. (16-18), we can obtain the temporal and spatial distribution of $c_I(\mathbf{r},t)$, $c_V(\mathbf{r},t)$, and $\eta_m(\mathbf{r},t)$ (m=1, 2, 3). We use the semi-implicit Fourier spectral method[58] for the time-stepping and spatial discretization. In the simulations, pure bcc Fe is considered. The dimensionless materials properties and model parameters are listed in Table 1.

Table I. Parameters used in the simulations.

Δt^*	0.002
T	600 K
T_0	673 K
A_L^*	64.5
w^*	0.013
M_I^*	1.
M_V^*	10^{-3}
L^*	1.0
c_I^{eq0}	$\exp(-4.8\times 11608.7/T)$
c_V^{eq0}	$\exp(-1.5\times 11608.7/T)$
κ^*	0.00
κ_1^*	0.085
λ_{ijkl}	$C_{44}=116, C_{11}=243, C_{12}=145$ (MPa)

2.2 Results and discussion

The interstitial loops with Burgers vectors $\mathbf{b} = a<100>$ on $\{100\}$ planes have a strong bias for interstitials such that their growth consumes interstitials in the matrix. Therefore, the growth kinetics of these interstitial loops is directly related to the loop bias or sink strength for interstitials. In the following sections, the developed phase-field model is used to study the effects on the interstitial loop growth kinetics of interstitial concentration, generation rate, recombination rate, sink strengths of other defects for vacancies and interstitials, and elastic interactions.

2.2.1 Stresses around an interstitial loop

Equation (13) describes stress-free strains associated with distributed interstitials, vacancies, and interstitial loops. The coefficients ε^{I0} and ε^{V0} are estimated by the formation volumes of the interstitials and vacancies as $\varepsilon^{I0} = (\Omega_I^0 - \Omega_0)/\Omega_0$ and $\varepsilon^{V0} = (\Omega_V^0 - \Omega_0)/\Omega_0$, respectively. Ω_0 is the atom volume in bcc Fe. Ω_I^0 and Ω_V^0 are the formation volumes of an interstitial and a vacancy, respectively, which can be obtained by MD simulations. As for the coefficient ε^{L0}, we determine it by comparing the stress field from MD simulations and linear elasticity. The stresses obtained from MD simulations and from linear elasticity with $\varepsilon^{L0} = 0.9$ are shown in Figure 1. The MD simulations were carried out in a cubic box of 40×40×30 unit cells containing 96000 atoms of α-Fe. An interstitial loop with the Burgers vector $\mathbf{b} = a[100]$ was initially set up by removing vacancies and inserting a [100] dumbbell (two interstitials) on each vacancy site for a given loop size; then, classical MD simulations were performed to relax the Fe system for 50 ps at 0 K, where periodic boundary conditions were applied to all three directions. The pair interaction and the many-body function for Fe−Fe interaction are described using Ackland and Mendelev potentials.[59] After relaxation, the atomic structure of the dislocation loop, the stress field and the displacement around the loop were evaluated. The linear elastic solution was from our phase-field calculation. The results show overall agreement except at the dislocation core when $\varepsilon^{L0} = 0.9$. Therefore, $\varepsilon^{L0} = 0.9$ is used in the following simulations.

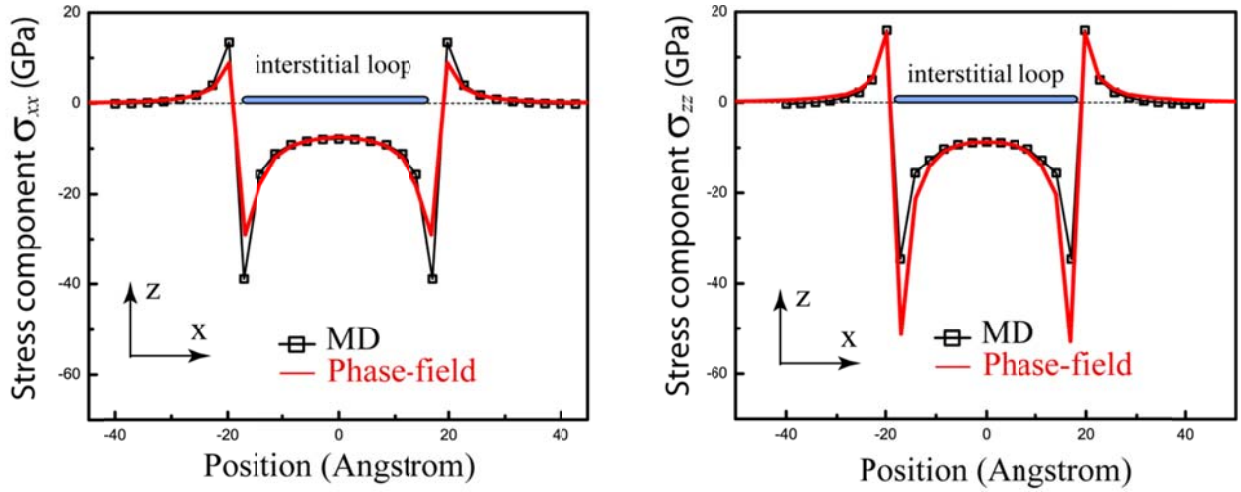

Figure 1. Stress distributions obtained from the MD simulation and phase-field modeling based on linear elasticity.

2.2.2 Effect of elastic interaction on growth kinetics of interstitial loops during aging

Interstitials, vacancies, and interstitial loops cause local volume change and generate local stresses. The elastic interactions among interstitial loops, interstitials, and vacancies affect the diffusion of interstitials and vacancies, and hence the growth kinetics of interstitial loops. Figure 2 presents the temporal evolution of an interstitial loop obtained from our 3-D simulations. Their two-dimensional (2-D) projections on the interstitial loop plane are also given. In the simulation, a small interstitial loop with a

radius $R_0 = 8l_0$ and Burgers vector $\mathbf{b} = a[100]$ on a (100) plane was placed at the center of a $96l_0 \times 96l_0 \times 64l_0$ simulation cell. The initial concentrations of $c_I^0 = c_V^0 = 0.01$ in the matrix were used, and the generation rate, recombination rate and sink strength for both interstitials and vacancies were set to be zero in the simulations. The shadowed region in Figure 2 represents the interstitial loop extent where the interstitial concentration is equal to 1. The interstitial concentration sharply goes to the equilibrium concentration of $c_I^{eq0}(T)$ outside the loop. As seen in the figure, the growth rate in <100> directions is slightly larger than that in <110> directions in the interstitial loop plane. As a result, the shape of the loop changes from a circle to a square with rounded corners. The growth anisotropy is attributed to the anisotropic elastic constants of bcc Fe which cause an anisotropic stress field and elastic interaction around the loop.

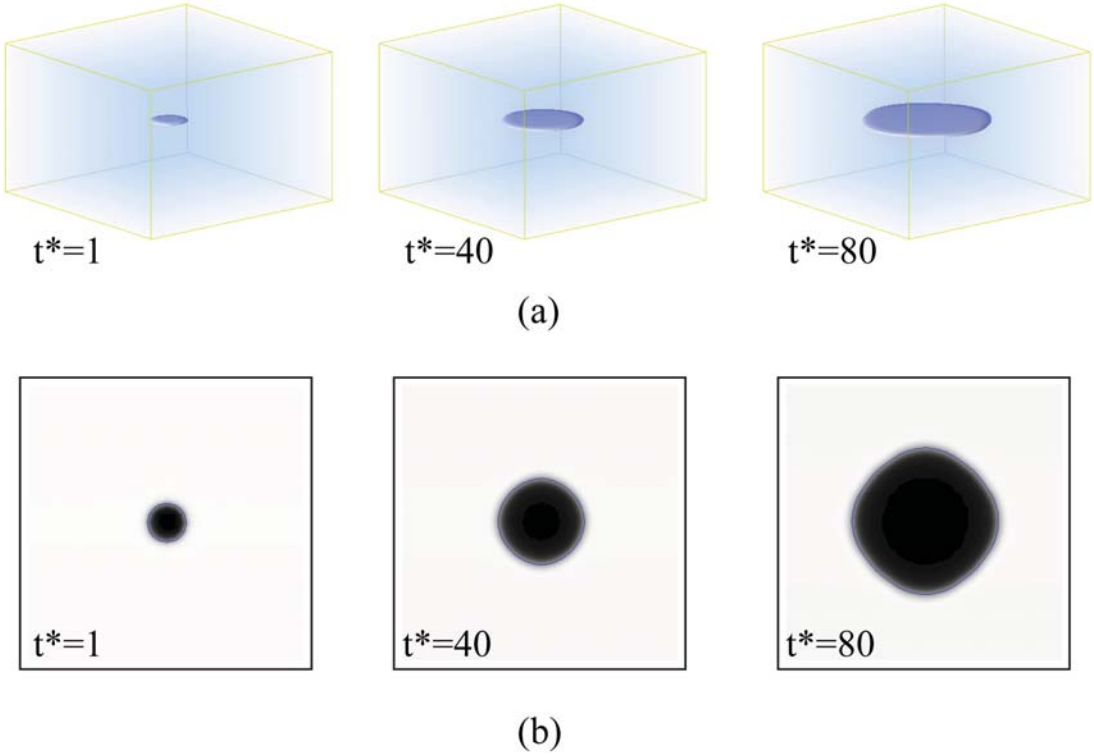

Figure 2. Snapshots of the morphology evolution of an interstitial loop during aging (a) in three dimensions; and (b) the projection on the plane of the interstitial loop.

The growth of an interstitial loop without elastic interaction is also simulated for comparison. The results suggest that the interstitial loop grows isotropically without elastic interaction. For the both cases, the radius *R* of the interstitial loop along [100] and [110] directions and the total area *S* of the interstitial loop versus time are plotted in Figure 3. It shows that a linear relationship ($R^* = R_0^* + At^*$) between the radius of the interstitial loop and time exists for the both cases with and without elastic interaction. A linear growth rate of the interstitial loop radius was observed in Fe-16Cr-14Ni alloys under electron radiation[60] and was theoretically predicted for plate-like precipitates under diffusion-controlled growth.[61]

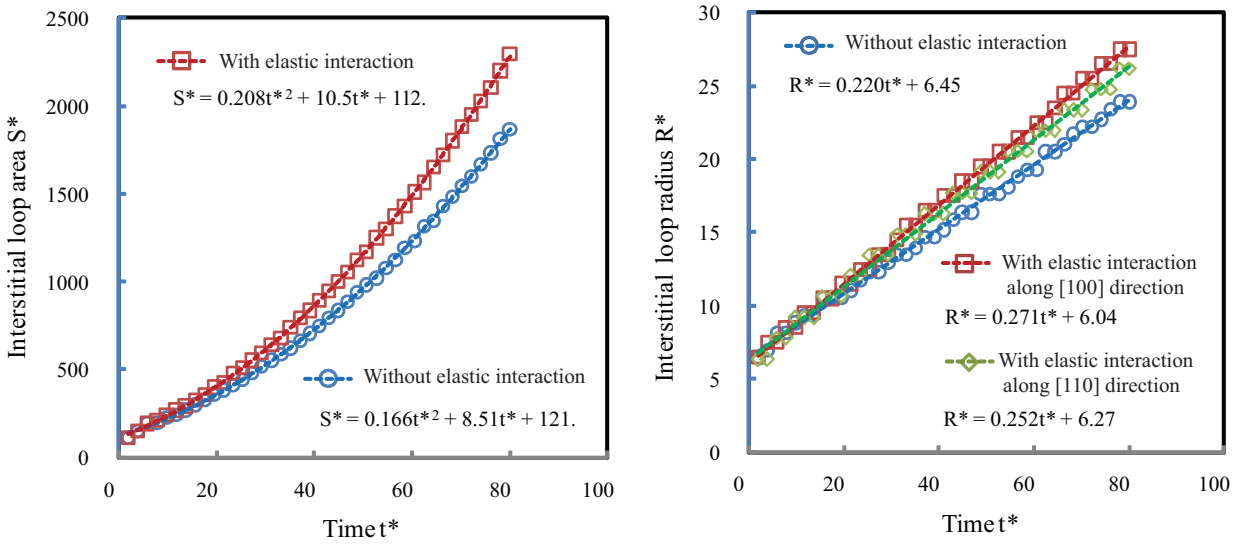

Figure 3. Interstitial loop area and radius versus time during aging.

2.2.3 Effect of interstitial concentrations on the growth kinetics during aging

With the same simulation cell above, the evolution of interstitial loops as a function of initial interstitial and vacancy concentrations with and without elastic interaction is simulated. The results are presented in Figures 4 and 5 for $c_I^0 = c_V^0 = 0.01$, 0.005, and 0.0025. The total area of the interstitial loop can be fitted by a quadratic function of time as $S^* = S_0 + S_1 t^* + S_2 t^{*2}$. This indicates that dS^*/dt^* is linear versus time. dS^*/dt^*, the absorption of interstitials per unit time t^*, is directly related to the sink strength of the interstitial loop for interstitials. Figure 5a shows that dS^*/dt^* and the average radius of the interstitial loop have a linear relationship of $dS^*/dt^* \sim AR^*$. Fitting the coefficient A in terms of the interstitial supersaturation $(c_I^0 - c_I^{eq0})$, we found that A is proportional to $(c_I^0 - c_I^{eq0})$ as shown in Figure 5b.

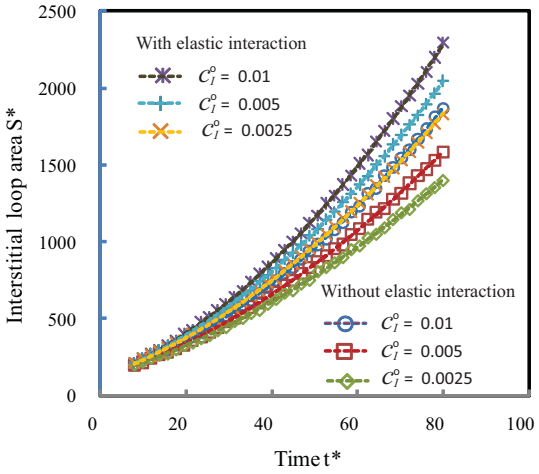

Figure 4. Size of an interstitial loop versus time for different initial interstitial concentrations.

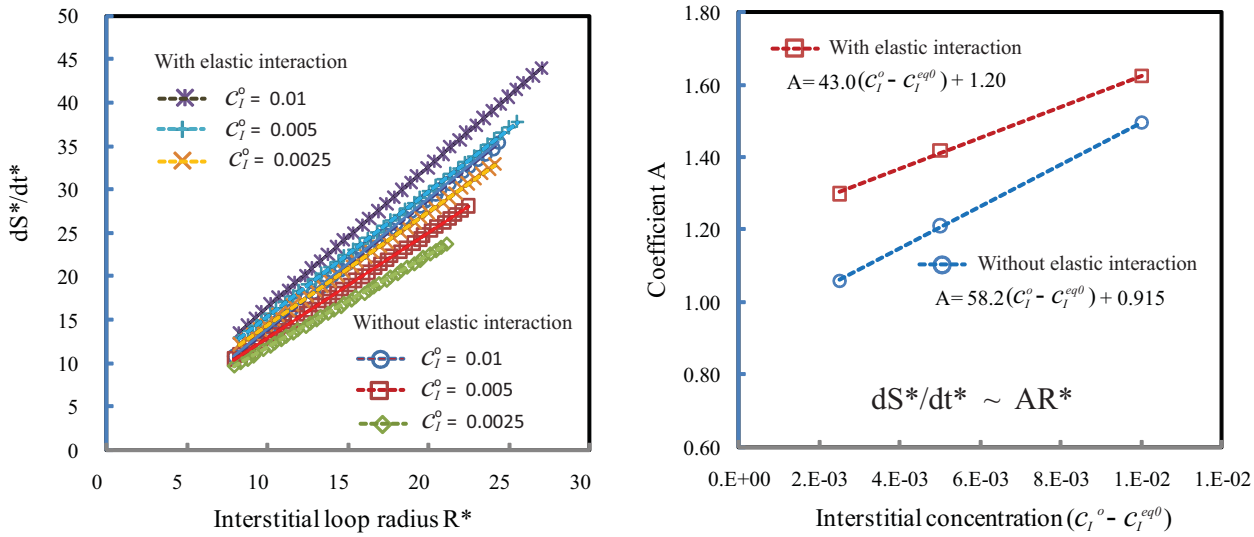

Figure 5. (a) dS^*/dt^* versus R^* for different initial interstitial concentrations during aging, with R^* and S^* being the average radius and area of an interstitial loop, respectively. (b) Coefficient A of $dS^*/dt^* \sim AR^*$ is linear versus $(c_I^0 - c_I^{eq0})$.

2.2.4 Effect of the interstitial generation rate on the interstitial loop growth kinetics

The generation rates of interstitials ($\dot{g}_I^*$) and vacancies ($\dot{g}_V^*$) are proportional to the rate of displacement per atom (dpa). The effect of the generation rates on the interstitial loop growth kinetics is simulated, and the results are presented in Figure 6. In the simulations, both the initial interstitial and vacancy concentrations were set to be 10^{-5} and their generation rates change within a large range from $\dot{g}_I^* = \dot{g}_V^* = 10^{-3}$ to 10^{-6}. Their recombination and sinks were ignored. The elastic interaction was taken into account. The results in Figure 6(a) show that a larger generation rate results in a faster growth rate. Similar to the aging process, a linear relationship of $dS^*/dt^* \sim BR^*$ also holds equal under irradiation with different dpa rates. Interstitial loop growth in pure Fe under electron irradiation at different temperatures follows a nearly linear relationship between loop radius and dpa.[35] The variation of coefficient B versus the interstitial generation rate $\dot{g}_I^*$ is plotted in Figure 6(b). Their relationship can be approximately expressed by $B = 0.154\ln(\dot{g}_I^*) + 2.95$.

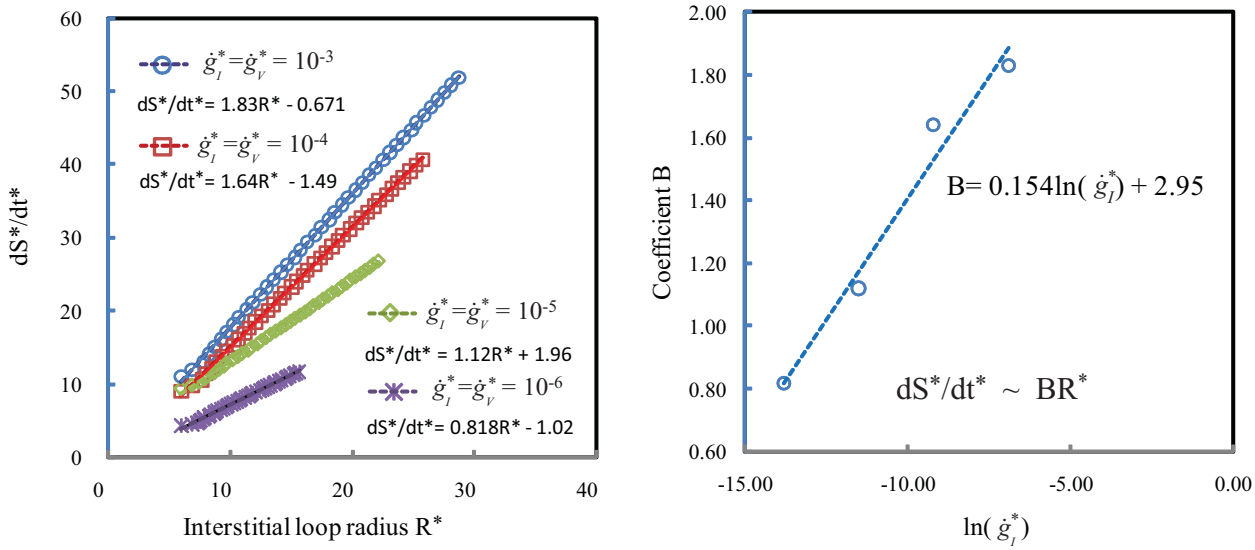

Figure 6. (a) dS^*/dt^* versus R^* for different generation rates under irradiation, with R^* and S^* being the average radius and area of an interstitial loop, respectively. (b) Coefficient B of $dS^*/dt^* \sim BR^*$ is approximately linear to $\ln(\dot{g}_I^*)$.

2.2.5 Effect of recombination rate and sink strength on the growth kinetics

Figure 7(a) displays the growth kinetics of an interstitial loop varying with the recombination rate between interstitials and vacancies. The simulation parameters were set as: $c_I^0 = c_V^0 = 0.01$, $\dot{g}_I^* = \dot{g}_V^* = 0.0$, and $k_I^* = k_V^* = 0.0$, but $\gamma^* =$ 0, 1, 3, 6, 10, 15, and 30. As expected, the growth rate decreases as the recombination rate increases. Figure 7(b) demonstrates the effect of sink strengths of other defects for vacancies and interstitials on the growth kinetics of the interstitial loop. The results were obtained by varying $k_I^* = k_V^* =$ 0, 50, and 200 under $c_I^0 = c_V^0 = 10^{-5}$, $\dot{g}_I^* = \dot{g}_V^* = 10^{-3}$, and $\gamma^* = 10$. Because both the recombination between interstitials and vacancies and the absorption of interstitials and vacancies at sinks reduce the vacancy and interstitial concentrations in the matrix, it is expected that the interstitial loop growth rate will decrease as the recombination rate and/or sink strength increases.

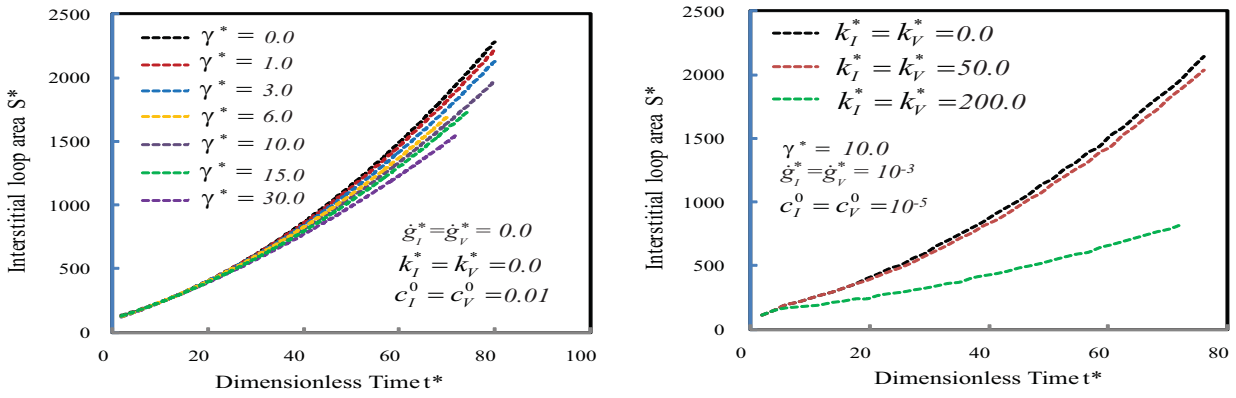

Figure 7. Interstitial loop size versus time for different recombination rates (a) and different sink strengths (b).

In summary, a phase-field model has been developed to simulate the growth kinetics of interstitial loops in irradiated materials. The interstitial loop with a Burgers vector $\mathbf{b} = a < 100 >$ on a $\{100\}$ plane of bcc Fe was studied. The thermodynamic and kinetic properties of defects such as formation energy, migration energy, and formation volumes of defects in bcc Fe were used to determine the model parameters. The stresses of an interstitial loop obtained through molecular dynamic simulations were employed to determine the stress-free strains of an interstitial loop. The evolution of an interstitial loop during aging and irradiation was simulated. The results show that 1) the elastic interaction speeds up the loop growth kinetics; 2) the elastic interaction also causes anisotropic growth rates; 3) the loop growth follows a linear growth rate, i.e., $dS^*/dt^* \sim AR^*$ or $R^* \sim At^*$ during aging and irradiation, which is in agreement with experimental observation. The effect of defect concentration, generation rate, recombination rate, sink strength, and elastic interaction on the interstitial loop growth kinetics is investigated separately, which demonstrates the advantage of simulations. The simulations show that the developed phase-field model is capable of studying the effect of thermodynamic and kinetic properties of defects and irradiation conditions on the sink strength of interstitial loops for interstitials.

3. PART II: THERMODYNAMIC AND KINETIC MODELS OF IRRADIATED FE-CR ALLOYS

Fe-Cr alloys have been used or considered for use in fast fission and fusion reactors due to their superior swelling resistance, high creep-rupture strengths, and good oxidation and corrosion resistance at elevated temperatures. A major concern for Fe-Cr alloys in nuclear reactors is the effect of irradiation on fracture. Neutron irradiation might cause a variety of microstructure changes such as solute segregation, precipitation, precipitate dissolution, and formation of voids and gas bubbles. All the microstructure changes affect mechanical properties such as strength, fracture toughness, and ductile-brittle transition temperature. The microstructure evolution in alloy systems during irradiation at elevated temperatures is

determined by a number of factors including 1) coupled transport of the solute atoms by point-defect fluxes to and away from sinks, such as grain boundaries, free surfaces, dislocation loops and interfaces between precipitate and matrix; 2) the inverse Kirkendall effect, whereby the faster-diffusing species exchange more often with the irradiation-induced vacancies migrating to sinks than slow-diffusing species. The fast-diffusing solutes are therefore depleted at sinks while the concentrations of the slow-diffusing species increase; 3) prior grain size and morphology, dislocation density, and precipitate size distribution; and 4) radiation conditions and temperatures.

Extensive experimental and theoretical results on microstructure evolution, thermodynamic and kinetic properties of Fe-Cr alloys are available in the literature.[62, 63] Therefore, Fe-Cr alloy is a good model alloy to demonstrate the capability of the phase-field modeling. Next we present a generic phase-field model describing multiple microstructure evolution phenomena in irradiated Fe-Cr alloys.

3.1 Generic phase-field model of microstructure evolution in irradiated Fe-Cr alloys

"Microstructures" refers to the compositional and structural inhomogeneity. A phase-field model describes a microstructure, (both the compositional/structural domains and interfaces), as a whole by using a set of field variables. The field variables are continuous across the interface regions, and hence the interfaces in a phase-field model are diffuse. There are two types of field variables, conserved and nonconserved. Conserved variables have to satisfy the local conservation condition. In irradiated bcc Fe-Cr alloys, neutron irradiation generates vacancies at the host bcc lattices, and Fe and Cr interstitials at interstitial lattices. Vacancies and interstitials may form their respective clusters. We assume that 1) mobile point defects and defect clusters are replaced by single vacancies or single interstitials with equivalent concentration and mobility; 2) immobile vacancy clusters act as void nuclei; 3) immobile interstitial clusters act as the nuclei of interstitial loops; and 4) mobile interstitials have <110> dumbbell configuration which is the energetically favorable in pure bcc Fe as well as in dilute and concentrated Fe-Cr alloys.. If solute segregation, voids, interstitial loops, and Cr-rich precipitates are considered simultaneously, two sets of field variables are required to describe the microstructure: one set of conserved variables $(c_i(\mathbf{r},t),\ i=1,2,...,n)$ describing the concentrations of vacancies, Fe atoms, and Cr atoms at the host bcc lattices and interstitial lattices, respectively, and the other set of nonconserved variables $(\eta_p(\mathbf{r},t),\ p=1,2,...,m)$ describing structural inhomogeneity including grain orientation $(p=1,2,...,g, g\le m)$, voids $(p=g+1)$, Cr-rich precipitates $(p=g+2)$, and (100) interstitial loops $(p=g+3,\ g+4, g+5)$. At equilibrium, the order parameters $(\eta_p(\mathbf{r},t),\ p=1,2,...,m)$ are zero in the matrix while they are equal to 1 inside their respective domains. For instance, $\eta_{g+1}(\mathbf{r},t)=1$ and $\eta_p(\mathbf{r},t)=0, p\ne g+1$ inside the voids, and $\eta_{g+1}(\mathbf{r},t)=0$ outside the voids. The concentrations $(c_i(\mathbf{r},t),\ i=1,2,...,n)$ have their equilibrium concentrations in each phase at equilibrium. For the inhomogeneous microstructure system described by conserved field variables $(c_i(\mathbf{r},t),\ i=1,2,...,n)$ and nonconserved field variables $(\eta_i(\mathbf{r},t),\ i=1,2,...,m)$, the total free energy can be calculated by

$$F = \int_V \left[f(c_1, c_2, ..., c_n, \eta_1, \eta_2, ..., \eta_m, T) + \sum_{i=1}^{n} \kappa_i (\nabla c_i)^2 + \sum_{p=1}^{m} \sum_{i,j=1}^{3} \left(\kappa_{ij} \frac{\partial \eta_p}{\partial r_i} \frac{\partial \eta_p}{\partial r_j} \right) \right] dV + \int_V \int_{V'} G(\mathbf{r} - \mathbf{r}') dV dV', \quad (19)$$

where f is the local free energy density, and κ_i and κ_{ij} are the gradient energy coefficients. The first volume integral represents the contribution to the free energy from short-range chemical interactions and the interfacial energy from the gradient terms. The second integral represents the contributions of long-range interactions to the total free energy, such as elastic interactions, electrostatic interactions. Both short and long-range interactions depend on the field variables.

With the total free energy of a microstructure discussed above, the evolution of field variables can be obtained by solving the following Cahn-Hilliard and Allen-Cahn equations,

$$\frac{\partial c_i(\mathbf{r},t)}{\partial t} = \nabla \cdot \left[M_{ij} \nabla \frac{\delta F}{\delta c_j(\mathbf{r},t)} \right] + \dot{g}_i^c(\mathbf{r},t) + \dot{R}_i^c(\mathbf{r},t) + \dot{S}_i^c(\mathbf{r},t) + \xi_i^c(\mathbf{r},t), \quad (20)$$

$$\frac{\partial \eta_p(\mathbf{r},t)}{\partial t} = -L_{pq} \frac{\delta F}{\delta \eta_p(\mathbf{r},t)} + \dot{g}_p^{\eta}(\mathbf{r},t), \quad (21)$$

where M_{ij} and L_{pq} are related to atom or defect mobility and interface mobility, respectively. $\dot{g}_i^c$, $\dot{R}_i^c$, $\dot{S}_i^c$ and ξ_i^c are the generation rate, recombination rate, sink strength, and fluctuation of atom or defect c_i, respectively. $\dot{g}_p^{\eta}$ is the generation rate of defect cluster η_p $(p = g+1, ..., m)$.

3.2 Thermodynamic and kinetic properties

Modeling the microstructure evolution using the phase-field approach is reduced to finding solutions to the kinetic equations (20, 21) together with long-range interaction and boundary conditions. The reliability of simulation results depends on the thermodynamic and kinetic properties used in the model including the reaction kinetics of irradiation defects and the local free energy of each phase existing in the system.

3.2.1 Reaction kinetics of irradiation defects

The reaction kinetics of irradiation defects required in phase-field models are listed below:

- generation rate $\dot{g}_i^c$ of point defects
- recombination rate $\dot{R}_i^c$ of interstitials and vacancies
- sink strength $\dot{S}_i^c$ for mobile defects

- generation rate $\dot{g}_p^{\eta}$ of immobile defect clusters
- migration energy and mobility M_{ij} of defects
- interfacial energy and interface mobility L_{pq}
- formation energy and solubility of defects
- formation volume of defects, etc.

Actually most of these properties of defects have been used in mean field methods[15, 64]. Therefore, the same formulism can be directly plugged into the phase field modeling. Speaking in general, atomistic simulations can provide all these data used in phase-field models.

3.2.2 Local free-energy formulation in phase-field model

One of the key components in a phase-field model is the local free-energy density function. For a given system, if free energies of different phases are valid from thermodynamic calculations such as CALPHAD, these free energies can be directly employed in the phase-field model. However, the local free energy of irradiated materials is usually not available in the literature. We have to develop the free energy density function based on the thermodynamic properties of the system. In Fe-Cr alloys under irradiation, multiple phases usually coexist. The matrix phase coexists with voids, Cr-rich precipitates, and interstitial loops. Define $f_M(c_1, c_2, ..., c_n, T)$ and $f_p(c_1, c_2, ..., c_n, T)$, with $(p = 1, 2, ..., m)$, as the free energies of the matrix phase and the different second phases, respectively. By using the Kim's formulation,[26] the chemical free energy as a function of the concentrations and order parameters is described as

$$\begin{aligned} & f(c_1, c_2, ..., c_n, \eta_1, \eta_2, .., \eta_m, T) \\ & = \sum_{p=1}^{m} \{h(\eta_p) f_M(c_1, c_2, ..., c_n, T) + [1 - h(\eta_p)] f_p(c_1, c_2, ..., c_n, T)\} + g(\eta_1, \eta_2, .., \eta_m), \end{aligned} \tag{22}$$

where $h(\eta_p) = 3\eta_p^2 - 2\eta_p^3$ is a shape function that represents the volume fraction of the matrix and the second phase p at a spatial point $\mathbf{r}$. $g(\eta_1, \eta_2, .., \eta_m) = \sum_m w_m \eta_m^2 (1 - \eta_m^2)$ is a double-well potential with respect to η_m, and w_m is the height of the corresponding double well.

3.2.3 Two-sublattice free energy model of irradiated Fe-Cr alloys

For low concentrations of alloy atoms and irradiation defects, the local free energy $f_M(c_1, c_2, ..., c_n, T)$ and $f_p(c_1, c_2, ..., c_n, T)$ can be described approximately by ideal and regular solution formulas such as Eqs. (6-7). But for high concentrations of alloy atoms and radiation defects, the excess Gibbs energy of mixing due to clustering and short-range ordering becomes important. In this case, the sublattice free energy formulism has been extensively used in thermodynamic calculations such as CALPHAD.[52] We suggest using the two-sublattice model shown in Figure 8 to describe the irradiated Fe-Cr alloys. In the

model, one sublattice is the host bcc lattice, and the other one is the interstitial lattice. Both sublattices are occupied by *Fe*, *Cr* and vacancy (*V*). The two sublattices are denoted by $(Fe,Cr,V)_{z_H}$, $(Fe,Cr,V)_{z_I}$ where *H* refers to host lattice, and *I* denotes interstitial lattice. Subscripts z_H and z_I are the lattice fractions of the host lattices and interstitial lattices, respectively, and satisfy $z_H + z_I = 1$. Assume c_{Fe}^H, c_{Cr}^H, c_V^H, and c_{Fe}^I, c_{Cr}^I, c_V^I are the lattice fractions of *Fe*, *Cr*, and vacancies at the host lattices and the interstitial lattices, respectively. They have the relationship: $c_{Fe}^H + c_{Cr}^H + c_V^H = 1$ and $c_{Fe}^I + c_{Cr}^I + c_V^I = 1$. The corresponding Gibbs free energy per mole can be expressed as

$$G_{mf} = G_{mf}^{\phi} + \Delta^{id} G_{mf}^{mix} + \Delta^{xs} G_{mf}^{mix} \tag{23}$$

with

$$\begin{aligned} G_{mf}^{\phi} &= c_{Fe}^H c_{Fe}^I G_{Fe:Fe}^{\phi} + c_{Fe}^H c_{Cr}^I G_{Fe:Cr}^{\phi} + c_{Fe}^H c_V^I G_{Fe:V}^{\phi} \\ &+ c_{Cr}^H c_{Fe}^I G_{Cr:Fe}^{\phi} + c_{Cr}^H c_{Cr}^I G_{Cr:Cr}^{\phi} + c_{Cr}^H c_V^I G_{Cr:V}^{\phi} \\ &+ c_V^H c_{Fe}^I G_{V:Fe}^{\phi} + c_V^H c_{Cr}^I G_{V:Cr}^{\phi} + c_V^H c_V^I G_{V:V}^{\phi}, \end{aligned} \tag{24}$$

where G^{ϕ} with subscripts is the Gibbs energy of the two sublattice structure (denoted as ϕ) with one element in each sublattice, called end-members. The second term of Eq. (23) ($\Delta^{id} G_{mf}^{mix}$) is the ideal mixing energy. Ideal mixing assumes mechanical mixing among atoms in each sublattice without interactions between atoms, i.e., all atomic bonds are identical. There is thus only an entropic contribution from the random distribution of atoms in each sublattice, i.e.,

$$\Delta^{id} G_{mf}^{mix} = RT \sum_{s=H,I} z_s \sum_{q=Fe,Cr,V} c_q^s \ln c_q^s, \tag{25}$$

where the first summation goes over all sublattices and the second summation goes over all constitutions in the corresponding sublattice.

In real materials, the atomic bonding characteristics between different atoms is unique, and the atomic mixing would thus result in additional Gibbs energy change with preferred local atomic arrangements, i.e., short-range ordering. This can cause miscibility gaps, order-disorder transitions, or the formation of compounds depending on the sign and magnitude of the excess Gibbs energy of the mixing $\Delta^{xs} G_{mf}^{mix}$. The widely used mathematical formula for $\Delta^{xs} G_{mf}^{mix}$ is the Redlich-Kister polynomial shown below:[65]

$$\begin{aligned} \Delta^{xs} G_{mf}^{mix} &= c_{Fe}^I [c_{Fe}^H c_{Cr}^H \sum_m L_{Fe,Cr:Fe}^m (c_{Fe}^H - c_{Cr}^H)^m + c_{Fe}^H c_V^H \sum_m L_{Fe,V:Fe}^m (c_{Fe}^H - c_V^H)^m \\ &\quad + c_{Cr}^H c_V^H \sum_m L_{Cr,V:Fe}^m (c_{Cr}^H - c_V^H)^m] \\ &\quad + c_{Cr}^I [c_{Fe}^H c_{Cr}^H \sum_m L_{Fe,Cr:Cr}^m (c_{Fe}^H - c_{Cr}^H)^m + c_{Fe}^H c_V^H \sum_m L_{Fe,V:Cr}^m (c_{Fe}^H - c_V^H)^m \\ &\quad + c_{Cr}^H c_V^H \sum_m L_{Cr,V:Cr}^m (c_{Cr}^H - c_V^H)^m] \end{aligned}$$

$$
\begin{aligned}
&+ c_V^I[c_{Fe}^H c_{Cr}^H \sum_m L_{Fe,Cr:V}^m (c_{Fe}^H - c_{Cr}^H)^m + c_{Fe}^H c_V^H \sum_m L_{Fe,V:V}^m (c_{Fe}^H - c_V^H)^m \\
&\quad + c_{Cr}^H c_V^H \sum_m L_{Cr,V:V}^m (c_{Cr}^H - c_V^H)^m] \\
&+ c_{Fe}^H[c_{Fe}^I c_{Cr}^I \sum_m L_{Fe:Fe,Cr}^m (c_{Fe}^I - c_{Cr}^I)^m + c_{Fe}^I c_V^I \sum_{m1} L_{Fe:Fe,V}^m (c_{Fe}^I - c_V^I)^m \\
&\quad + c_{Cr}^I c_V^I \sum_{m1} L_{Fe:Cr,V}^m (c_{Cr}^I - c_V^I)^m] \\
&+ c_{Cr}^H[c_{Fe}^I c_{Cr}^I \sum_m L_{Cr:Fe,Cr}^m (c_{Fe}^I - c_{Cr}^I)^m + c_{Fe}^I c_V^I \sum_m L_{Cr:Fe,V}^m (c_{Fe}^I - c_V^I)^m \\
&\quad + c_{Cr}^I c_V^I \sum_{m1} L_{Cr:Cr,V}^m (c_{Cr}^I - c_V^I)^m] \\
&+ c_V^H[c_{Fe}^I c_{Cr}^I \sum_m L_{V:Fe,Cr}^m (c_{Fe}^I - c_{Cr}^I)^m + c_{Fe}^I c_V^I \sum_m L_{V:Fe,V}^m (c_{Fe}^I - c_V^I)^m \\
&\quad + c_{Cr}^I c_V^I \sum_m L_{V:Cr,V}^m (c_{Cr}^I - c_V^I)^m] + \cdots
\end{aligned}
\tag{26}
$$

where L^m with subscripts is the m^{th} binary interaction parameter. The colons separate constitutions between sublattices and commas separate interacting constitutions in the same sublattice. In Eq. (25), only the binary interaction terms are listed. If higher accuracy is required, the short range ordering (SRO) and ternary interactions have to be considered.

In principle, the parameters appeared in Eqs. (24,25) can be determined by the formation energies of the end compounds, defects and different defect clusters. Atomistic simulations are able to provide these formation energies.

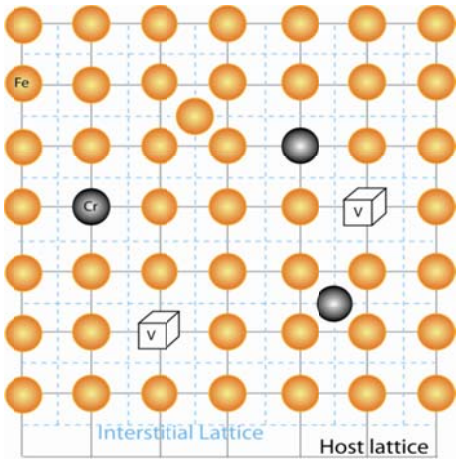

Figure 8. Schematic illustration of two sublattices.

4. SUMMARY AND OUTLOOK

Phase-field methods have been applied to simulate the evolution of different microstructures such as gas bubbles in polycrystallines, void lattice formation due to 1-D migration of SIAs, void migration under a temperature gradient, void swelling, and interstitial loop growth in irradiated materials. The simulation results demonstrate that the developed phase-field models can qualitatively predict the microstructure evolution kinetics observed in experiments. Therefore, future efforts are expected to focus on the development of quantitative phase-field models. The development of a quantitative phase-field model relies on not only a correct description of the microstructure evolution processes, but also accurate thermodynamic and kinetic databases. These databases, in principle, can be obtained from atomistic simulations. For specific fuel and reactor materials in practical applications, significant efforts are required to develop approaches in linking phase-field models with existing or future thermodynamic and kinetic databases.

The assessment of phase-field models is also a challenge because of the specific time and length scales and complicated microstructure evolution occurring in the irradiated materials. However, specific experimental measurements are required on the microstructure and microstructure evolution kinetics for evaluating the prediction of phase-field simulations.

Figure 9 shows the time and length scales of phase-field modeling in the multiscale simulation methods used currently. One of the important objectives of phase-field modeling is to provide the thermodynamic and kinetic properties of microstructure evolution for macroscale modeling. To achieve the goal, standard formats are expected for phase-field modeling output of microstructures, relationships between microstructure and properties, and evolution kinetics of microstructures and properties. It is also expected to extend the phase-field models to simulate multi-phase evolution and multi-material processes that take place in irradiated materials. Therefore, increasing efforts should be devoted in developing scalable parallel codes and in performing large-scale simulations in order to provide statistical and uncertainty quantification of simulation results.

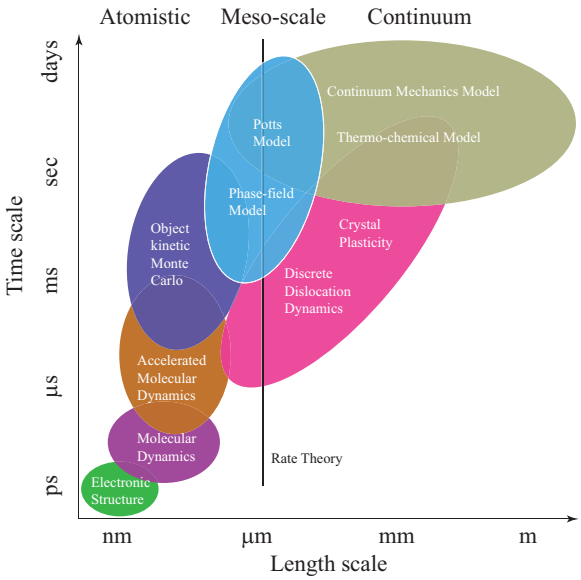

Figure 9. Time and length scales of multiscale simulation methods.

REFERENCES

1 Evans JH. Observations of a regular void array in high purity molybdenum irradiated with 2 Mev nitrogen ions. Nature, 1971, 229: 403-404

2 Kulcinski GL, Brimhall JL, Kissinge HE. Production of voids in nickel with high energy selenium ions. Journal of Nuclear Materials, 1971, 40: 166-174

3 Zinkle SJ, Singh BN. Microstructure of Cu-Ni alloys neutron irradiated at 210 degrees C and 420 degrees C to 14 dpa. Journal of Nuclear Materials, 2000, 283: 306-312

4 Bacon DJ, Gao F, Osetsky YN. The primary damage state in fcc, bcc and hcp metals as seen in molecular dynamics simulations. Journal of Nuclear Materials, 2000, 276: 1-12

5 Fu CC, Willaime F, Ordejon P. Stability and mobility of mono- and di-interstitials in alpha-Fe. Physical Review Letters, 2004, 92: 175503

6 Gao F, Bacon DJ, Osetsky YN, et al. Properties and evolution of sessile interstitial clusters produced by displacement cascades in alpha-iron. Journal of Nuclear Materials, 2000, 276: 213-220

7 Osetsky YN, Bacon DJ, Serra A, et al. One-dimensional atomic transport by clusters of self-interstitial atoms in iron and copper. Philosophical Magazine, 2003, 83: 61-91

8 Heinisch HL, Singh BN, Golubov SI. A kinetic Monte Carlo study of mixed 1D/3D defect migration. Journal of Computer-Aided Materials Design, 1999, 6: 277-282

9 Soneda N, Ishino S, Takahashi A, et al. Modeling the microstructural evolution in bcc-Fe during irradiation using kinetic Monte Carlo computer simulation. Journal of Nuclear Materials, 2003, 323: 169-180

10 Wirth BD, Bringa EM. A kinetic Monte Carlo model for helium diffusion and clustering in fusion environments. Physica Scripta, 2004, T108: 80-84

11 Domain C, Becquart CS, Malerba L. Simulation of radiation damage in Fe alloys: an object kinetic Monte Carlo approach. Journal of Nuclear Materials, 2004, 335: 121-145

12 Sizmann R. Effect of radiation upon diffusion in metals. Journal of Nuclear Materials, 1978, 69-70: 386-412

13 Mansur LK. Theory and experimental background on dimensional changes in irradiated alloys. Journal of Nuclear Materials, 1994, 216: 97-123

14 Woo CH, Singh BN, Garner FA. Production bias - a proposed modification of the driving force for void swelling under cascade damage conditions. Journal of Nuclear Materials, 1992, 191: 1224-1228

15 Singh BN, Foreman AJE. Production bias and void swelling in the transient regime under cascade damage conditions. Philosophical Magazine A-Physics of Condensed Matter Structure Defects and Mechanical Properties, 1992, 66: 975-990

16 Trinkaus H, Singh BN, Foreman AJE. Glide of interstitial loops produced under cascade damage conditions - possible effects on void formation. Journal of Nuclear Materials, 1992, 199: 1-5

17 Golubov SI, Singh BN, Trinkaus H. Defect accumulation in fee and bcc metals and alloys under cascade damage conditions - Towards a generalisation of the production bias model. Journal of Nuclear Materials, 2000, 276: 78-89

18 Barashev AV, Golubov SI, Trinkaus H. Reaction kinetics of glissile interstitial clusters in a crystal containing voids and dislocations. Philosophical Magazine A-Physics of Condensed Matter Structure Defects and Mechanical Properties, 2001, 81: 2515-2532

19 Trinkaus H, Heinisch HL, Barashev AV, et al. 1D to 3D diffusion-reaction kinetics of defects in crystals. Physical Review B, 2002, 66: 060105

20 Singh BN, Eldrup M, Zinkle SJ, et al. On grain-size-dependent void swelling in pure copper irradiated with fission neutrons. Philosophical Magazine A-Physics of Condensed Matter Structure Defects and Mechanical Properties, 2002, 82: 1137-1158

21 Tikare V, Braginsky M, Bouvard D, et al. Numerical simulation of microstructural evolution during sintering at the mesoscale in a 3D powder compact. Computational Materials Science, 2010, 48: 317-325

22 Chen LQ. Phase-field models for microstructure evolution. Annual Review of Materials Research, 2002, 32: 113-140

23 Cha PR, Kim SG, Yeon DH, et al. A phase field model for the solute drag on moving grain boundaries. Acta Materialia, 2002, 50: 3817-3829

24 Gronhagen K, Agren J. Grain-boundary segregation and dynamic solute drag theory - A phase-field approach. Acta Materialia, 2007, 55: 955-960

25 Li YL, Hu SY, Liu ZK, et al. Effect of substrate constraint on the stability and evolution of ferroelectric domain structures in thin films. Acta Materialia, 2002, 50: 395-411

26 Kim SG, Kim WT, Suzuki T. Phase-field model for binary alloys. Physical Review E, 1999, 60: 7186-7197

27 Guyer JE, Boettinger WJ, Warren JA, et al. Phase field modeling of electrochemistry. I. Equilibrium. Physical Review E, 2004, 69: 021603

28 Hu SY, Henager CH, Geelhood KJ, et al. Phase-field modeling of microstructure and thermal conductivity evolution under radiation. Transactions of the American Nuclear Soceity 2008, 98: 1130-1131

29 Hu SY, Henager CH, Heinisch HL, et al. Phase-field modeling of gas bubbles and thermal conductivity evolution in nuclear fuels. Journal of Nuclear Materials, 2009, 392: 292-300

30 Hu SY, Henager CH. Phase-field modeling of void lattice formation under irradiation. Journal of Nuclear Materials, 2009, 394: 155-159

31 Hu SY, Henager CH. Phase-field simulation of void migration in a temperature gradient. Acta Materialia, 2010, 58: 3230-3237

32 Li YL, Hu SY, Sun X, et al. Phase-field modeling of void migration and growth kinetics in materials under irradiation and temperature field. Journal of Nuclear Materials, 2010, 407: 119-125

33 Li YL, Hu SY, Sun X, et al. Phase-field modeling of void evolution and swelling in materials under irradiation. Science China: Physics, Mechanics & Astronomy, 2011, 54: 856-865

34 Suganuma K, Kayano H. Dislocation loops in electron-irradiated ferritic stainless-steel. Radiation Effects and Defects in Solids, 1981, 54: 81-86

35 Ward AE, Fisher SB. Dislocation loop growth in pure iron under electron-irradiation. Journal of Nuclear Materials, 1989, 166: 227-234

36 Masters BC. Dislocation loops in irradiated iron. Philosophical Magazine, 1965, 11: 881-893

37 Kiritani M, Yoshida N, Takata H, et al. Growth of interstitial type dislocation loops and vacancy mobility in electron-irradiated metals. Journal of the Physical Society of Japan, 1975, 38: 1677-1686

38 Bacon DJ, Delarubia TD. Molecular dnamics computer simulations of displacement cascades in metals. Journal of Nuclear Materials, 1994, 216: 275-290

39 Osetsky YN, Bacon DJ, Serra A, et al. Stability and mobility of defect clusters and dislocation loops in metals. Journal of Nuclear Materials, 2000, 276: 65-77

40 Little EA, Bullough R, Wood MH. On the swelling resistance of ferritic steel. Proceedings of the Royal Society of London Series A-Mathematical Physical and Engineering Sciences, 1980, 372: 565-579

41 Braislford AD, Bullough R. Void growth and its relation to intrinsic point-defect properties. Journal of Nuclear Materials, 1978, 69-70: 434-450

42 Marian J, Wirth BD, Perlado JM. Mechanism of formation and growth of < 100 > interstitial loops in ferritic materials. Physical Review Letters, 2002, 88: 255507

43 Eyre BL, Bullough R. On formation of interstitial loops in bcc metals. Philosophical Magazine, 1965, 12: 31-39

44 Wirth BD. How does radiation damage materials? Science, 2007, 318: 923-924

45 Cahn JW. On spinodal decomposition. Acta Metallurgica, 1961, 9: 795-801

46 Norgett MJ, Robinson MT, Torrens IM. Proposed method of calculating displacement dose-rates. Nuclear Engineering and Design, 1975, 33: 50-54

47 Leffers T, Singh BN. On the recombination rate of irradiation-induced interstitials and vacancies. Journal of Nuclear Materials, 1980, 91: 336-342

48 Brailsfo AD, Bullough R. Rate theory of swelling due to void growth in irradiated metals. Journal of Nuclear Materials, 1972, 44: 121-135

49 Galimov RR, Goryachev SB. The sink strength of dislocation multipole and dislocation wall. Physica Status Solidi B-Basic Research, 1989, 154: 43-54

50 Allen SM, Cahn JW. Microscopic theory for antiphase boundary motion and its application to antiphase domain coarsening. Acta Metallurgica, 1979, 27: 1085-1095

51 Sundman B, Agren J. A regular solution model for phases with several components and sub-lattices, suitable for computer-applications. Journal of Physics and Chemistry of Solids, 1981, 42: 297-301

52 Liu ZK. First-principles calculations and CALPHAD modeling of thermodynamics. Journal of Phase Equilibria and Diffusion, 2009, 30: 517-534

53 Woodward C, Rao SI. Ab-initio simulation of isolated screw dislocations in bcc Mo and Ta. Philosophical Magazine A-Physics of Condensed Matter Structure Defects and Mechanical Properties, 2001, 81: 1305-1316

54 Cai W, Bulatov VV, Chang JP, et al. Anisotropic elastic interactions of a periodic dislocation array. Physical Review Letters, 2001, 86: 5727-5730

55 Li J, Wang CZ, Chang JP, et al. Core energy and Peierls stress of a screw dislocation in bcc molybdenum: A periodic-cell tight-binding study. Physical Review B, 2004, 70: 104113

56 Khachaturian AG. Theory of Structural Transformations in Solid. Canada: John Wiley & Sons. Inc, 1983

57 Hu SY, Chen LQ. A phase-field model for evolving microstructures with strong elastic inhomogeneity. Acta Materialia, 2001, 49: 1879-1890

58 Chen LQ, Shen J. Applications of semi-implicit Fourier-spectral method to phase field equations. Computer Physics Communications, 1998, 108: 147-158

59 Ackland GJ, Mendelev MI, Srolovitz DJ, et al. Development of an interatomic potential for phosphorus impurities in alpha-iron. Journal of Physics-Condensed Matter, 2004, 16: S2629-S2642

60 Ohnuki S. private communication,

61 Porter DA, Easterling KE. Phase Transitions in Metals and Alloys. New York: Chapman & Hall, 1992

62 Andersson JO, Sundman B. Thermodynamic properties of the Cr-Fe system. Calphad-Computer Coupling of Phase Diagrams and Thermochemistry, 1987, 11: 83-92

63 Xiong W, Selleby M, Chen Q, et al. Phase Equilibria and Thermodynamic Properties in the Fe-Cr System. Critical Reviews in Solid State and Materials Sciences, 2010, 35: 125-152

64 Woo CH, Singh BN. Production bias due to clustering of point-defects in irradiation-induced cascades. Philosophical Magazine A-Physics of Condensed Matter Structure Defects and Mechanical Properties, 1992, 65: 889-912

65 Redlich O, Kister AT. Algebraic representation of thermodynamic properties and the classification of solutions. Industrial and Engineering Chemistry, 1948, 40: 345-348

ACKNOWLEDGMENTS

This work was supported by the U. S. Department of Energy's Nuclear Energy Advanced Modeling and Simulation (NEAMS) Program at the Pacific Northwest National Laboratory, which is operated by Battelle for the U. S. Department of Energy under Contract No. DE-AC05-76RL01830. The authors acknowledge valuable discussions with Fei Gao and C. H. Henager, Jr.